Available online at www.sciencedirect.com
ScienceDirect
Trans. Nonferrous Met. Soc. China 28(2018) 1970−1979
Transactions of Nonferrous Metals Society of China
www.tnmsc.cn

Effect of Mo addition on microstructure, ordering, and room-temperature mechanical properties of Fe−50Al

Mehmet YILDIRIM[1], M. Vedat AKDENIZ[2], Amdulla O. MEKHRABOV[2]

1. Department of Metallurgical and Materials Engineering, Selcuk University, Konya 42130, Turkey;
2. Novel Alloys Design and Development Laboratory (NOVALAB), Department of Metallurgical and Materials Engineering, Middle East Technical University, Ankara, Turkey

Received 20 December 2017; accepted 15 March 2018

Abstract: The effects of Mo addition on microstructures, phase relationships, order–disorder phase-transition temperatures and room-temperature mechanical properties of $Fe_{50}Al_{50-n}Mo_n$ alloys (n=1, 3, 5, 7, and 9, mole fraction, %) were investigated after solidification and heat treatment. Structural characterization of the samples was performed via X-ray diffraction (XRD), scanning electron microscopy (SEM) and differential scanning calorimetry. Room-temperature mechanical properties were investigated by conducting compression and microhardness tests. Mo_3Al particles precipitated in all alloys because of the limited solid solubility of Mo in the Fe−Al-based phases. The as-cast $Fe_{50}Al_{50-n}Mo_n$ alloys exhibited brittle behavior with high yield strength and limited fracture strain at room temperature. Compared with the as-cast alloys, all the heat-treated alloys except for the $Fe_{50}Al_{41}Mo_9$ alloy exhibited enhanced mechanical properties at room temperature. The heat-treated $Fe_{50}Al_{43}Mo_7$ alloy exhibited the highest fracture strain and compressive strength of 25.4% and 2.3 GPa, respectively.
Key words: iron aluminides; microstructure; order–disorder phase transformation; compressive properties

1 Introduction

Fe−Al-based alloys are promising candidates for structural applications at elevated temperatures because of their excellent corrosion and oxidation resistance as well as their intermediate-temperature strength [1,2]. In addition, their low densities, relatively high melting points, and low cost compared with those of many commercial Fe-based alloys and stainless steels are advantageous [1−10]. The unique physical and mechanical properties of Fe−Al-based intermetallics are attributed to their long-range-ordered superlattices [1,2]. However, their poor ductility and brittleness at room temperature significantly hinder their fabricability and potential use for high-temperature structural applications [5−13].

The room- and high-temperature mechanical properties of Fe−Al-based alloys strongly depend on the deviation from alloy stoichiometry as well as the type and content of ternary alloying additions [14]. The addition of ternary alloys is one of the most effective ways to strengthen Fe−Al-based alloys through solid-solution hardening, precipitation hardening, and ordering [3,8,15]. The solid-solubility behavior of the ternary alloying element in the Fe−Al-based phase plays an important role in activating or hindering the strengthening mechanisms. Alloying additions such as Mo or W have very limited solid solubility in Fe−Al-based phases and usually lead to the formation of a secondary phase [8,9,16−18].

Many secondary phases in the Fe−Al−Mo system act as strengtheners, such as the hexagonal Fe_7Mo_6 phase (μ), cubic $A15$-type Mo_3Al phase, tetragonal $D0_{22}$-type Al_8FeMo_3 (τ_1) phase, and hexagonal Al_8Cr_5-type ε phase [19−21]. Among these phases, the cubic $A15$-type Mo_3Al phase is in equilibrium with both the α-(Fe,Al) phase and $B2$-type ordered FeAl intermetallic compound according to the isothermal sections of the Fe−Al−Mo ternary phase diagram at 1000 °C [19−22]. Such a two-phase Fe−Al−Mo alloy containing a relatively soft FeAl-based matrix phase and hard and brittle Mo_3Al particles may have several attractive properties because the mechanical properties can be easily enhanced by modifying the Al content, which controls the atomic ordering and thermal vacancy content in the Fe−Al-based

Corresponding author: Mehmet YILDIRIM; Tel: +90-332-2232021; Fax: +90-332-2410635; E-mail: ymehmet@selcuk.edu.tr
DOI: 10.1016/S1003-6326(18)64842-3

matrix, and the Mo content which controls the volume fraction of the hard and brittle Mo_3Al particles.

Although the effects of the Mo addition to $D0_3$-type ordered Fe_3Al and $B2$-type ordered Fe–40Al alloys have been examined in several experimental studies, little information is available on the structural properties, order–disorder phase-transition temperatures, and room-temperature mechanical properties of the Al-rich stoichiometric FeAl (Fe−50Al) intermetallic compound. Therefore, we investigated the effects of the Mo addition on the microstructure, phase relationships, $B2 \leftrightarrow A2$ order–disorder phase-transition temperatures, and room-temperature mechanical properties of $Fe_{50}Al_{50-n}Mo_n$ alloys (n=1, 3, 5, 7, and 9, mole fraction, %) after solidification and subsequent heat treatment. Moreover, our effort was directed toward establishing a relationship between the microstructure and room-temperature mechanical properties.

2 Experimental

The $Fe_{50}Al_{50-n}Mo_n$ alloys (n=1, 3, 5, 7, and 9, mole fraction, %) were prepared by arc melting using a non-consumable tungsten electrode and a water-cooled copper tray in a high-purity argon atmosphere. 10−15 g of samples were produced using high-purity constituent elements (99.97% Fe, 99.9% Al, and 99.95% Mo, mass fraction). Prior to arc melting the furnace chamber was evacuated to 10^{-3} Pa. Arc melting was then performed under an argon inert gas atmosphere. Each alloy was remelted several times to achieve greater composition homogeneity. The mass loss during the arc-melting process was less than 0.5% (mass fraction). $Fe_{50}Al_{50-n}Mo_n$ alloy cylindrical rods with diameter of 3 mm and length of 150 mm were fabricated via suction casting from the arc-melted ingots. The rods were homogenized at 900 °C for 24 h in encapsulated and argon-filled quartz tubes followed by an annealing heat treatment at 400 °C for 168 h.

X-ray diffraction (XRD) analyses were conducted using a Rigaku D/Max−2200 PC diffractometer with Cu K_α radiation (λ=1.54056 Å) and an X-ray source operating voltage of 40 kV to identify the phases present in the samples. XRD scans were performed in the 2θ range of 25°−100° using a scanning rate of 2 (°)/min. The microstructures were examined using scanning electron microscopy (SEM, JEOL JSM−6400) with a FEI Nova Nano 430 field-emission gun coupled with energy-dispersive X-ray spectrometry (EDS). The elemental compositions of the constituent phases were measured by averaging six EDS punctual data. The SEM samples were prepared using standard metallographic techniques and etched with a solution containing 68 mL of glycerin, 16 mL of 70% HNO_3, and 16 mL of 40% HF. The volume fractions of the phases observed in the metallographic examinations were calculated using the systematic manual point count procedure described in ASTM E562.

Differential scanning calorimetry (DSC) measurements were performed using a high-temperature thermal analyzer (Setaram SETSYS 16/18) at a heating rate of 10 °C/min under constant argon flow. Before the DSC measurements, the instrument was calibrated for a wide range of temperatures and scanning rates using high-purity standard elements of Al, Zn, Pb, Ag, Au, and Ni. The accuracy of the temperature calibration was ±1 °C.

The room-temperature mechanical properties of the as-cast and heat-treated $Fe_{50}Al_{50-n}Mo_n$ alloys were investigated by conducting compression tests using an Instron 5582 universal testing machine at a strain rate of 10^{-4} s^{-1} according to ASTM E9-09. Cylindrical specimens (3 mm in diameter, 4.5 mm in length) were cut using spark erosion, and any surface layers were removed by grinding before testing. The 0.2% proof stress in uniaxial compression was considered the yield stress. Eight specimens were tested for each condition. Samples showing deviations due to artifacts such as voids and cracks were excluded from the analysis. Vickers microhardness measurements were performed using a microhardness tester under a load of 500 g.

3 Results and discussion

3.1 Structural properties

The microstructures of the as-cast alloys (Fig. 1) consisted of equiaxed and coarse Fe−Al-based grains with second-phase particles distributed along the grain boundaries. However, after heat treatment, second-phase particles also precipitated within the grains for the alloys with higher Mo contents (n>3). The volume fraction of second-phase particles gradually increased with increasing Mo content, reaching a maximum for the alloy with the highest Mo content (n=9). These second-phase particles were identified as binary Mo_3Al precipitates (Cr_3Si-type ordered, space group 223, $Pm\bar{3}n$) in the XRD analyses (Fig. 2) and EDS measurements (Table 1). The diffraction peaks corresponding to the Mo_3Al phase first appeared for the heat-treated $Fe_{50}Al_{43}Mo_7$ composition, and the relative intensities of these peaks increased with increasing Mo content from 7% to 9%. The results of the EDS analyses also showed that some amount of Fe (4.3%) was dissolved in Mo_3Al phase. EUMANN et al [19] also reported that there is some Fe solubility in Mo_3Al phase. They studied Fe−40.5Al−5.7Mo composition and measured the Fe solubility in Mo_3Al phase as 4.8%.

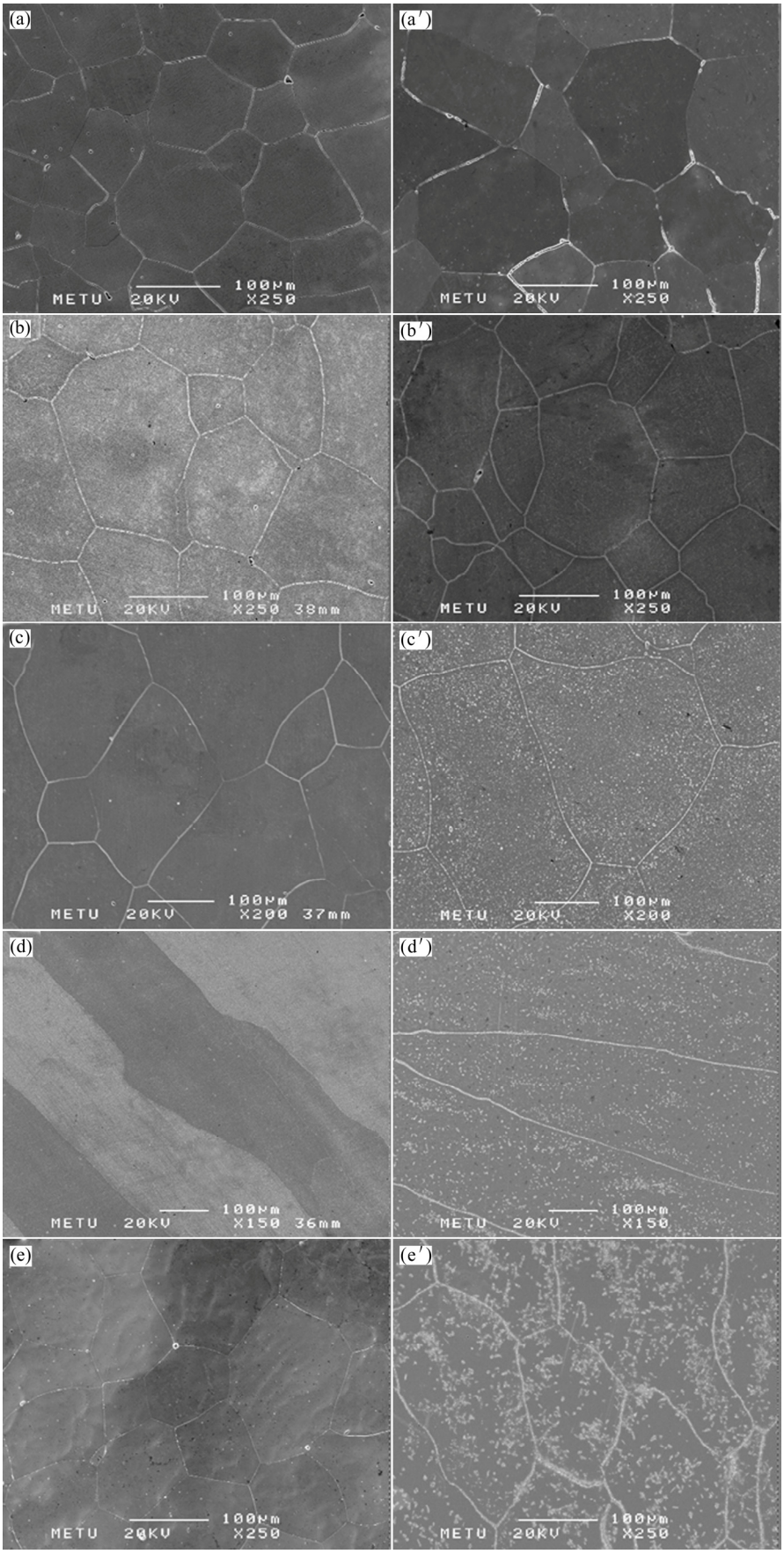

Fig. 1 SEM images of as-cast (a−e) and heat-treated (a′−e′) $Fe_{50}Al_{50-n}Mo_n$ alloys: (a, a′) n=1; (b, b′) n=3; (c, c′) n=5; (d, d′) n=7; (e, e′) n=9

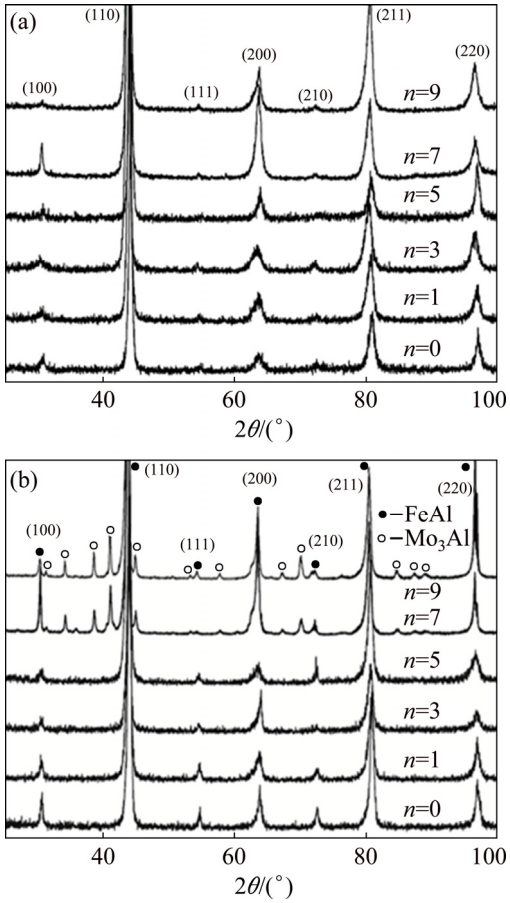

Fig. 2 XRD patterns of $Fe_{50}Al_{50-n}Mo_n$ alloys: (a) As-cast; (b) Heat-treated

Table 1 EDS analysis results of Mo_3Al precipitates

x(Mo)/%	*x*(Al)/%	*x*(Fe)/%
74.9 ± 1.1	20.7 ± 0.4	4.3 ± 0.4

The EDS analyses of the Fe−Al-based matrix phase (Table 2) revealed abundant Mo_3Al precipitation after heat treatment. In the alloys containing less than 7% Mo, good agreement was observed between the nominal and analyzed matrix compositions, whereas the Fe and Al contents deviated from the actual compositions for the heat-treated alloys containing 7% and 9% Mo because of the relatively high volume fraction of the Mo_3Al phase. Compared with the nominal compositions, the Fe content increased and the Al content decreased for these two compositions.

The precipitation of Mo_3Al after heat treatment is directly related to the solubility behavior of Mo in Fe−Al-based phase equilibrium with the Mo_3Al phase. The investigated compositions of the $Fe_{50}Al_{50-n}Mo_n$ alloys lie near/within the ($B2$ + Mo_3Al) two-phase region in the isothermal section of the Fe−Al−Mo ternary phase diagram at 1000 °C [21]. Heat treatment results in extra nucleation of Mo_3Al particles and the growth of existing particles for supersaturated as-cast alloys. In addition, the solubility of Mo in the $B2$-type ordered Fe−Al-based phase decreases with decreasing temperature during cooling [21,22]. Hence, the amount of Mo_3Al precipitates substantially increased with heat treatment followed by furnace cooling.

High-magnification FESEM analyses (Fig. 3) were performed to investigate the morphology, size, distribution, and volume fraction of Mo_3Al precipitates for the heat-treated $Fe_{50}Al_{43}Mo_7$ and $Fe_{50}Al_{41}Mo_9$ alloys. The volume fraction and size of the Mo_3Al precipitates for both alloys are summarized in Table 3. The volume fractions were in very good agreement with the expected amounts of Mo_3Al precipitates [22]. For example, EUMANN et al [22] presented the expected equilibrium amount of Mo_3Al as 5% for Fe−40.4Al−8.9Mo composition, while we found it is 5.5% for similar composition of Fe−41Al−9Mo. The Mo_3Al precipitates did not have any specific morphology and were uniformly distributed along grain boundaries and the grain interior without the formation of any precipitate-free zones.

Cooling to room temperature after annealing is known to lead to a $B2/A2$ order–disorder phase transformation of the Fe−Al-based matrix phase. In our previous study [23], we showed that the $B2/A2$ order–disorder phase-transformation temperature ($T^{B2/A2}$) for Fe−Al-based intermetallics strongly depends on the type and content of the ternary alloying addition.

Table 2 Nominal and measured compositions of $Fe_{50}Al_{50-n}Mo_n$ samples

Nominal composition/%	As-cast			Heat-treated		
	x(Fe)/%	*x*(Al)/%	*x*(Mo)/%	*x*(Fe)/%	*x*(Al)/%	*x*(Mo)/%
Fe−50Al	50.2 ± 0.1	49.8 ± 0.1	−	50.4 ± 0.2	49.6 ± 0.2	−
Fe−49Al−1Mo	50.2 ± 0.1	48.8 ± 0.2	1.2 ± 0.3	50.5 ± 0.3	48.4 ± 0.3	1.1 ± 0.2
Fe−47Al−3Mo	49.5 ± 0.3	47.4 ± 0.3	3.1 ± 0.4	49.0 ± 0.4	47.7 ± 0.6	3.3 ± 0.4
Fe−45Al−5Mo	49.2 ± 0.5	45.0 ± 0.3	5.8 ± 0.9	49.4 ± 0.2	45.0 ± 0.5	5.6 ± 0.9
Fe−43Al−7Mo	51.9 ± 0.8	40.9 ± 0.9	7.2 ± 0.9	59.2 ± 0.9	34.9 ± 1.4	5.9 ± 1.0
Fe−41Al−9Mo	50.8 ± 0.6	40.6 ± 1.0	8.6 ± 1.2	59.4 ± 1.1	34.1 ± 1.3	6.5 ± 1.4

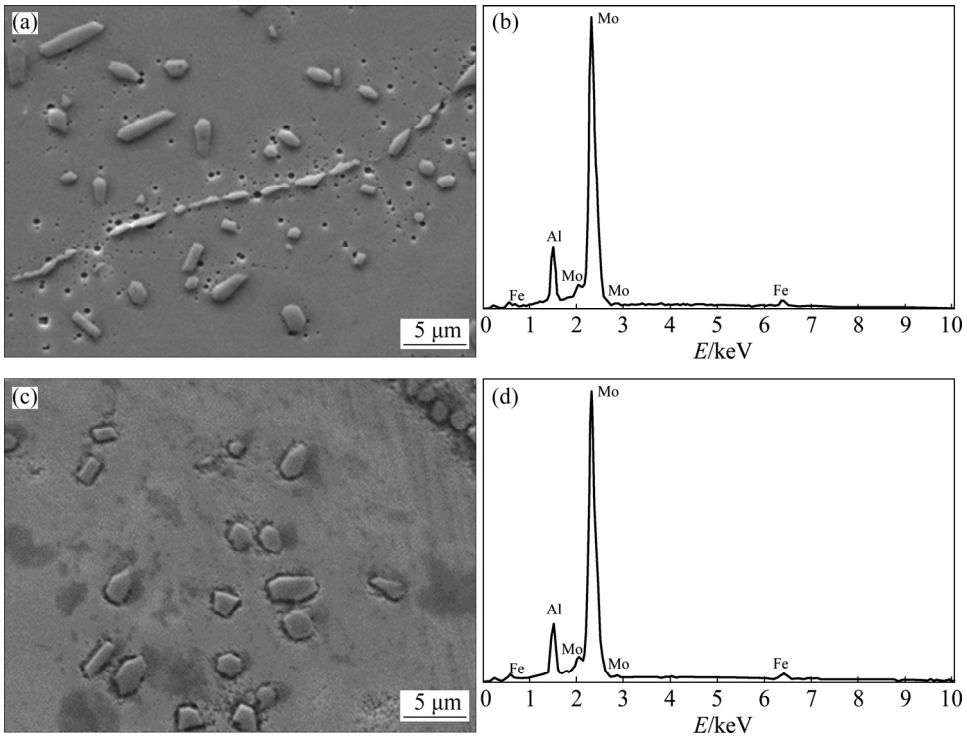

Fig. 3 FESEM micrographs (a, c) and EDS analyses (b, d) of heat-treated $Fe_{50}Al_{50-n}Mo_n$ alloys: (a, b) n=7; (b, c) n=9

Table 3 Size and volume fraction of Mo_3Al precipitates for heat-treated $Fe_{50}Al_{43}Mo_7$ and $Fe_{50}Al_{41}Mo_9$ alloys

x(Mo)/%	Precipitate size (grain interior)/μm	Precipitate size (grain boundary)/μm	Volume fraction of precipitate/%
7	2.1 ± 0.2	3.8 ± 0.8	2.2
9	2.7 ± 0.1	4.3 ± 0.7	5.8

Therefore, in the current work, DSC measurements were performed to investigate the effect of the addition of Mo on $T^{B2/A2}$ and the melting temperature of the FeAl intermetallic compound. The DSC heating curves for the heat-treated $Fe_{50}Al_{50-n}Mo_n$ alloys are presented in Fig. 4, and the measured $T^{B2/A2}$ and melting temperatures are listed in Table 4. The addition of 1% Mo led to an increase of $T^{B2/A2}$, whereas further increasing the Mo content (n>1) led to a strong decrease of $T^{B2/A2}$.

The effects of small ternary alloying additions (n≤1) on $T^{B2/A2}$ have been shown to be directly related to the relative partial ordering energy parameter β [23,24]. This parameter accounts for the effects of both the site occupancy behavior of the alloying element atoms and the magnitude of the partial ordering energies of the Al−X and Fe−X atomic pairs relative to the Fe−Al pairs. For the 1% Mo addition, the sign of the β parameter was much greater than unity (β≫1). Therefore, the Mo atoms preferentially substituted for Fe sublattice sites with very strong Al–Mo and Fe–Mo atomic bonds, indicating the higher potential to increase $T^{B2/A2}$. However, for larger Mo additions (n>1), the variation of $T^{B2/A2}$ can be directly attributed to the microstructural features.

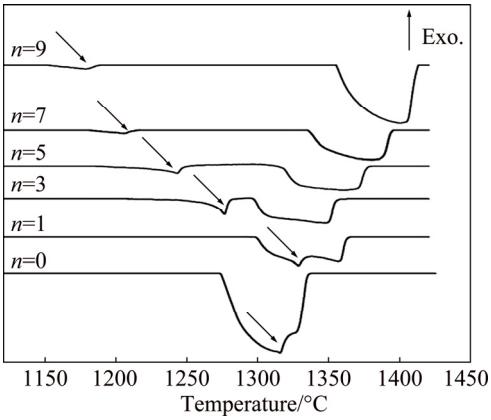

Fig. 4 DSC heating curves of heat-treated $Fe_{50}Al_{50-n}Mo_n$ alloys at heating rate of 10 K/min

Table 4 Experimentally measured order-disorder transition, solidus and liquidus temperatures of heat-treated $Fe_{50}Al_{50-n}Mo_n$ alloys

Alloy	$T^{B2\leftrightarrow A2}$/°C	T_{sol}/°C	T_{liq}/°C
FeAl	1316	1270	1325
Fe−49Al−1Mo	1330	1299	1346
Fe−47Al−3Mo	1274	1298	1347
Fe−45Al−5Mo	1244	1317	1365
Fe−43Al−7Mo	1205	1338	1384
Fe−41Al−9Mo	1178	1354	1408

The Al concentration in the Fe–Al-based matrix phase shifted toward lower values, for the heat-treated alloys containing 7% and 9% Mo because of the precipitation of the Mo_3Al phase. According to the binary Fe−Al phase diagram [25], $T^{B2/A2}$ decreases and the melting temperature increases when approaching the Fe-rich $D0_3$ side (lower Al content). However, a much lower reduction in $T^{B2/A2}$ was observed in the presence of solid-solution-forming alloying elements such as Cr and Mn compared with Mo [26]. Because Cr and Mn have extended solid solubility in the Fe−Al-based phase, no second-phase precipitation was observed. Thus, less reduction of $T^{B2/A2}$ was observed for the same Mo addition.

3.2 Room-temperature mechanical properties

3.2.1 As-cast $Fe_{50}Al_{50-n}Mo_n$ alloys

Figure 5 presents the room-temperature compressive stress–strain curves of the investigated $Fe_{50}Al_{50-n}Mo_n$ alloys. Compressive stress–strain curves for as-cast and heat-treated FeAl intermetallic compounds are also provided for comparison. The stoichiometric FeAl intermetallic compound exhibited brittle behavior with limited compressive plasticity and an ultrahigh yield strength. The yield strength decreased and the compressive fracture strain showed an increasing tendency with increasing Mo or decreasing Al content. Among the as-cast ternary alloys, the $Fe_{50}Al_{50-n}Mo_n$ alloys with 1% and 3% Mo exhibited similar mechanical properties as the binary as-cast FeAl. These two compositions also exhibited low fracture strain and high yield strength at room temperature.

Compared with the alloys containing 1% and 3% Mo, the $Fe_{50}Al_{50-n}Mo_n$ alloys (n>3) alloys exhibited considerably higher compressive ductility at room temperature. These alloys also exhibited lower yield strength and higher compressive strength. However, the reasonably higher compressive ductility of these compositions compared with those of the $Fe_{50}Al_{49}Mo_1$ and $Fe_{50}Al_{47}Mo_3$ alloys was mainly attributed to the softening that arises from decreasing the Al content. In Fe–Al-based alloys, ductility is directly related to the thermal vacancy content, which is directly related to the Al content. Theoretical and experimental studies have shown that the number of thermally generated vacancies increases with increasing Al content, reaching a maximum near the stoichiometric composition [27,28]. XIAO and BAKER [27] also reported that the yield strength reached a maximum value for the stoichiometric Fe−50Al composition. Therefore, the stoichiometric and near-stoichiometric compositions exhibited more brittle behavior than the other compositions. The microhardness values for the investigated as-cast $Fe_{50}Al_{50-n}Mo_n$ alloys are listed in Table 6. The indentations were positioned

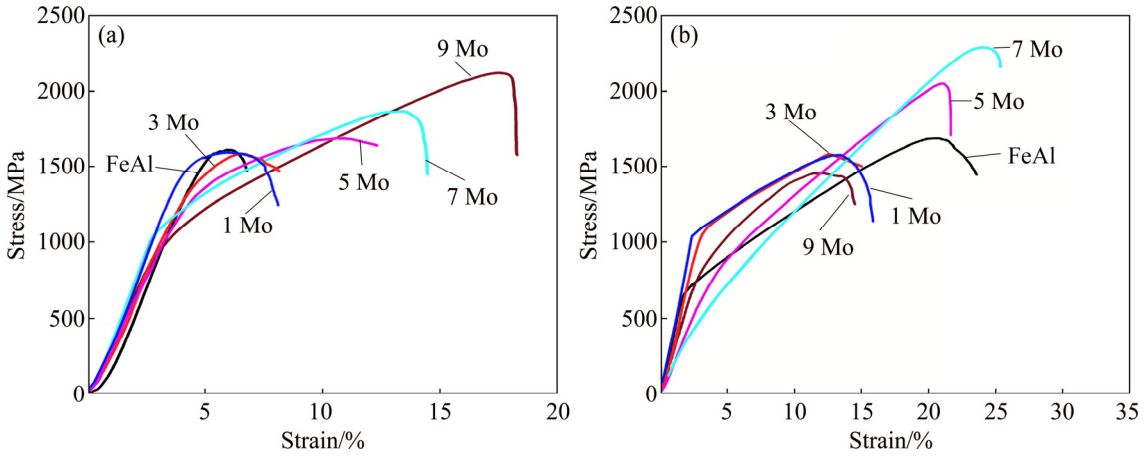

Fig. 5 Room temperature stress−strain compression curves of $Fe_{50}Al_{50-n}Mo_n$ alloys: (a) As-cast; (b) Heat-treated

Table 5 Mechanical properties for as-cast and heat-treated $Fe_{50}Al_{50-n}Mo_n$ alloys (yield stress σ_y (0.2% offset), ultimate compressive stress σ_{max} and fracture strain ε_f)

Alloy	As-cast			Heat-treated		
	σ_y/MPa	σ_{max}/MPa	e_f/%	σ_y/MPa	σ_{max}/MPa	e_f/%
FeAl	1449 ± 92	1657 ± 69	6.8 ± 0.5	673 ± 55	1687 ± 46	23.6 ± 0.6
Fe−49Al−1Mo	1297 ± 97	1581 ± 95	8.2 ± 0.5	949 ± 87	1492 ± 46	15.9 ± 0.4
Fe−47Al−3Mo	1255 ± 89	1606 ± 101	8.1 ± 0.7	1019 ± 85	1583 ± 51	15.0 ± 0.4
Fe−45Al−5Mo	1140 ± 78	1749 ± 98	12.3 ± 1.0	633 ± 75	2095 ± 89	21.6 ± 0.4
Fe−43Al−7Mo	1130 ± 69	1890 ± 107	14.3 ± 1.1	504 ± 54	2295 ± 98	25.4 ± 0.6
Fe−41Al−9Mo	1059 ± 72	2180 ± 114	18.3 ± 1.2	745 ± 46	1515 ± 49	14.5 ± 0.6

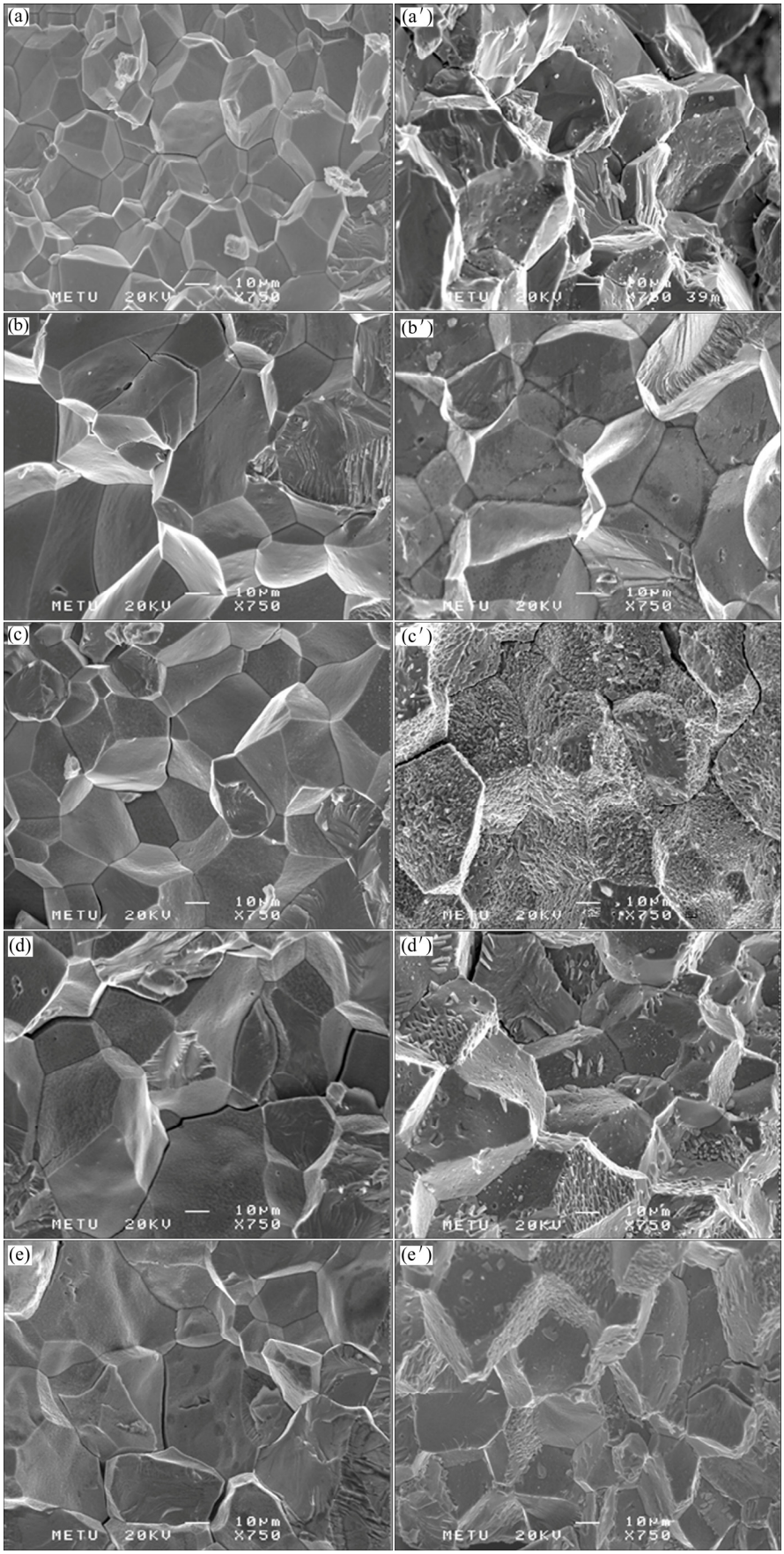

Fig. 6 Fracture surfaces of as-cast (a−e) and heat-treated (a′−e′) $Fe_{50}Al_{50-n}Mo_n$ alloys after compressive testing: (a, a′) n=1; (b, b′) n=3; (c, c′) n=5; (d, d′) n=7; (e, e′) n=9

off the grain boundaries to avoid effects from the Mo_3Al precipitates at the grain boundary. Similar trends as those for the compression tests were observed. The as-cast $Fe_{50}Al_{50-n}Mo_n$ alloys with Mo content below 5% had much higher hardness than the $Fe_{50}Al_{50-n}Mo_n$ alloys containing 5%−9% Mo. The softening of the $Fe_{50}Al_{50-n}Mo_n$ alloys (n≥5) is also attributed to the effect of the Al content of the Fe−Al-based matrix phase. Moreover, fractographic observations of the as-cast $Fe_{50}Al_{50-n}Mo_n$ alloys (Fig. 6) revealed that all the samples failed by intergranular decohesion.

3.2.2 Heat-treated $Fe_{50}Al_{50-n}Mo_n$ alloys

Uniaxial compressive stress–strain curves for the heat-treated $Fe_{50}Al_{50-n}Mo_n$ alloys are presented in Fig. 5(b). The room-temperature mechanical properties of the binary stoichiometric FeAl intermetallic compound significantly improved after annealing. Heat treatment resulted in a reduction of the yield strength from 1449 to 673 MPa and an increase of the compressive fracture strain from 6.8% to 23.6% (Table 5). However, the mechanical properties of the ternary $Fe_{50}Al_{50-n}Mo_n$ alloys after heat treatment were highly composition dependent. Among the heat-treated alloys, $Fe_{50}Al_{43}Mo_7$ alloy exhibited the optimal mechanical properties with the highest compressive strength and fracture strain of 2.3 GPa and 25.4%, respectively, and a yield strength of 504 MPa. In contrast, the $Fe_{50}Al_{41}Mo_9$ alloy with the highest Mo content exhibited the lowest fracture strain of 14.5%, which was even lower than the as-cast value. Moreover, this alloy exhibited the second-lowest compressive strength of 1.5 GPa.

Table 6 Microhardness values for as-cast and heat-treated $Fe_{50}Al_{50-n}Mo_n$ alloys

Alloy	Microhardness	
	As-cast	Heat-treated
FeAl	506 ± 92	392 ± 46
Fe−49Al−1Mo	547 ± 97	402 ± 46
Fe−47Al−3Mo	564 ± 89	413 ± 51
Fe−45Al−5Mo	537 ± 78	367 ± 89
Fe−43Al−7Mo	447 ± 69	320 ± 98
Fe−41Al−9Mo	392 ± 72	427 ± 49

The hardness of the heat-treated $Fe_{50}Al_{50-n}Mo_n$ alloys increased with 1% and 3% Mo and then decreased upon further increasing the Mo content to 5% or 7%. Eventually, hardness reached the maximum value for the alloy containing 9% Mo because of the exclusive Mo_3Al formation and growth within the grains and at the grain boundaries. The heat-treated $Fe_{50}Al_{45}Mo_5$ and $Fe_{50}Al_{43}Mo_7$ alloys exhibited higher compressive plasticity and lower strength and hardness than expected ones based on the rule of mixtures. This anomaly can be explained by the effect of the Al content of the Fe−Al-based matrix phase. The stoichiometric Fe−50Al and near-stoichiometric Fe−49Al and Fe−48Al compositions were the most brittle compositions among the Fe−Al-based alloys with $B2$- or $D0_3$-type ordered crystal structures [27,28]. The strength and hardness decreased and the ductility increased with decreasing Al content. In addition, fractographic observations of the heat-treated $Fe_{50}Al_{50-n}Mo_n$ alloys (Fig. 6) revealed that all the samples failed by intergranular decohesion without any sign of plastic deformation.

Interestingly, the heat-treated binary FeAl intermetallic compound exhibited the second-highest compressive fracture strain while being the most brittle composition in the as-cast state. To further evaluate the mechanical properties of the heat-treated $Fe_{50}Al_{50-n}Mo_n$ alloys, consideration of the microstructural properties and phase relationships was needed, and a strong relationship between the structural and mechanical properties needed to be established. First, the mechanical properties of the heat-treated $Fe_{50}Al_{50-n}Mo_n$ alloys depended on two main parameters: 1) the volume fraction of the hard and brittle Mo_3Al intermetallic phase and 2) the Al content of the Fe–Al-based matrix phase.

The fine Mo_3Al precipitates formed during cooling act as strong strengthening phases in Fe−Al-based alloys [19−22]. EUMANN et al [22] reported that the hardness of the brittle Mo_3Al particles is much higher than that of the Fe−Al-based phase both in the as-cast and heat-treated states. Therefore, it was expected that the yield strength and hardness of the heat-treated $Fe_{50}Al_{50-n}Mo_n$ alloys would increase with increasing Mo content because of the precipitation of Mo_3Al. However, the observed mechanical properties differed. For example, the $Fe_{50}Al_{43}Mo_7$ alloy was the softest composition despite the precipitation of Mo_3Al. Thus, the second-most important parameter, the Al content of the Fe−Al-based matrix phase, should be considered. The Al content of the heat-treated $Fe_{50}Al_{43}Mo_7$ alloy was much lower than that of the nominal composition, and a low Al content induces a softening effect. Moreover, this composition contained nearly 2% hard and brittle Mo_3Al particles, and these particles provide less strengthening. In contrast, the $Fe_{50}Al_{41}Mo_9$ alloy, containing nearly 6% hard and brittle Mo_3Al particles, was the most brittle composition among the heat-treated alloys investigated despite having the lowest Al content of the Fe−Al-based matrix phase.

In summary, it can be concluded that the Al content of the Fe−Al-based matrix phase is the dominant factor controlling the room-temperature mechanical properties of heat-treated $Fe_{50}Al_{50-n}Mo_n$ alloys containing a low amount of Mo_3Al precipitates. However, the volume fraction of hard and brittle Mo_3Al precipitates becomes the dominant factor controlling the room-temperature

mechanical properties when the amount of Mo_3Al particles reaches a certain limit such as in the heat-treated $Fe_{50}Al_{41}Mo_9$ alloy.

The room-temperature mechanical properties of $Fe_{50}Al_{50-n}Mo_n$ alloys show many similarities with those of the $Fe_{50}Al_{50-n}Nb_n$ alloys prepared in our previous study [29]. For both alloy systems, the ternary as-cast alloys containing 7% and 9% Mo (or Nb) exhibited the highest compressive fracture strain and strength compared with the other ternary alloys (n<7). Moreover, among the heat-treated alloys, the $Fe_{50}Al_{41}Mo_9$ and $Fe_{50}Al_{41}Nb_9$ alloys containing the highest amount of Mo or Nb exhibited the lowest compressive fracture strain.

4 Conclusions

1) All the investigated ternary alloys consisted of a Fe−Al-based phase and Mo_3Al second-phase particles.

2) For the as-cast alloys, the Mo_3Al particles were distributed along the grain boundaries.

3) Heat treatment led to a strong increase of the volume fraction of the Mo_3Al particles.

4) The volume fraction of the Mo_3Al particles increased with increasing Mo content, and the particles also precipitated within the grains for the heat-treated alloys.

5) The $B2/A2$ order–disorder phase-transformation temperature first decreased with the addition of 1% Mo and then decreased upon further increasing the Mo content.

6) Among the as-cast alloys, the $Fe_{50}Al_{41}Mo_9$ alloy with the highest Mo content exhibited the highest compressive strength and fracture strain of 2.18 GPa and 18.3%, respectively.

7) The compressive fracture strain of the $Fe_{50}Al_{50-n}Mo_n$ alloys, except for the $Fe_{50}Al_{41}Mo_9$ alloy, improved after heat treatment.

8) Among the heat-treated alloys, the $Fe_{50}Al_{43}Mo_7$ alloy exhibited the highest compressive strength and fracture strain of 2.3 GPa and 25.4%, respectively.

9) Promising properties of the Fe−Al−Mo alloys for structural applications were obtained. However, all the samples failed by intergranular decohesion. For this reason, further alloy design and development is needed. It is predicted that room-temperature mechanical properties can be further improved with C or B addition. Grain boundary strength will be enhanced with formation of strong boride or carbide particles at grain boundaries and brittle fracture can be hindered.

Acknowledgements

This paper was prepared from Ph.D. thesis of Mehmet Yildirim. The authors gratefully acknowledge ÖYP Program at Middle East Technical University and The Scientific and Technological Research Council of Turkey, TUBITAK, National Scholarship Programme for PhD Students.

References

[1] HARDWICK D, WALLWORK G. Iron-aluminum base alloys, A review of their feasibility as high temperature materials [J]. Review of High Temperature Material, 1978, 4: 47−74.

[2] YOO M H, SASS S L, FU C L, MILLS M J, DIMIDUK D M, GEORGE E P. Deformation and fracture of intermetallics [J]. Acta Metallurgica Et Materialia, 1993, 41: 987−1002.

[3] STOLOFF N S. Iron aluminides: Present status and future prospects [J]. Materials Science and Engineering A, 1998, 258: 1−14.

[4] STOLOFF N S, LIU C T, DEEVI S C. Emerging applications of intermetallics [J]. Intermetallics, 2000, 8: 1313−1320.

[5] RUAN Y, GU Q, LU P, WANG H, WEI B. Rapid eutectic growth and applied performances of Fe Al Nb alloy solidified under electromagnetic levitation condition [J]. Materials Design, 2016, 112: 239−245.

[6] RUAN Y, YAN N, ZHU H, ZHOU K, WEI B. Thermal performance determination of binary Fe−Al alloys at elevated temperatures [J]. Journal of Alloys and Compounds, 2017, 701: 676−681.

[7] DOBES F, VODICKOVA V, VESELY J. KRATOCHVIL P. The effect of carbon additions on the creep resistance of Fe−25Al−5Zr alloy [J]. Metallurgical and Materials Transactions A, 2016, 47: 6070−6076.

[8] PALM M. Concepts derived from phase diagram studies for the strengthening of Fe−Al-based alloys [J]. Intermetallics, 2005, 13: 1286−1295.

[9] STEIN F, PALM M, SAUTHOFF G. Mechanical properties and oxidation behaviour of two-phase iron aluminium alloys with $Zr(Fe,Al)_2$ Laves phase or $Zr(Fe,Al)_{12}$ τ_1 phase [J]. Intermetallics, 2005, 13: 1275−1285.

[10] LIU C T. Physical metallurgy and mechanical properties of ductile ordered alloys $(Fe, Co, Ni)_3V$ [J]. International Materials Reviews, 1984, 29: 168−194.

[11] BAKER I, GAYDOSH D J. Flow and fracture of Fe−Al [J]. Materials Science and Engineering, 1987, 96: 147−158.

[12] GAYDOSH D J, DRAPER S L, NATHAL M V. Microstructure and tensile properties of Fe−40 At. pct Al alloys with C, Zr, Hf, and B additions [J]. Metallurgical Transactions A, 1989, 20: 1701−1714.

[13] BALIGIDAD R, RADHAKRISHNA A, DATTA A, RAO V R. Effect of molybdenum addition on structure and properties of high carbon Fe_3Al based intermetallic alloy [J]. Materials Science and Engineering A, 2001, 313: 117−122.

[14] TITRAN R H, VEDULA K M, ANDERSON G G. High temperature properties of equialomic FeAl with ternary additions [C]//Materials Research Society Symposium Proceedings 1985. Pittsburgh, PA: MRS, 1985: 309−317.

[15] MORRIS D G. Possibilities for high-temperature strengthening in iron aluminides [J]. Intermetallics, 1998, 6: 753−758.

[16] WASILKOWSKA A, BARTSCH M, STEIN F, PALM M, SZTWIERTNIA K, SAUTHOFF G, MESSERSCHMIDT U. Plastic deformation of Fe−Al polycrystals strengthened with Zr-containing Laves phases: I. Microstructure of undeformed materials [J]. Materials Science and Engineering A, 2004, 380: 9−19.

[17] RISANTI D D, SAUTHOFF G. Strengthening of iron aluminide alloys by atomic ordering and Laves phase precipitation for high-temperature applications [J]. Intermetallics, 2005, 13: 1313−1321.

[18] SAUTHOFF G. Multiphase intermetallic alloys for structural applications [J]. Intermetallics, 2000, 8: 1101−1109.

[19] EUMANN M, SAUTHOFF G, PALM M. Phase equilibria in the Fe−Al−Mo system. Part I: Stability of the Laves phase Fe_2Mo and isothermal section at 800 °C [J]. Intermetallics, 2008, 16: 706−716.
[20] EUMANN M, SAUTHOFF G, PALM M. Phase equilibria in the Fe−Al−Mo system. Part II: Isothermal sections at 1000 and 1150 °C [J]. Intermetallics, 2008, 16: 834−846.
[21] EUMANN M. Phasengleichgewichte und mechanicses Verhalten im ternaren Legierungssystem Fe−Al−Mo [D]. Aachen, Germany: Shaker-Verlag, 2002: 120−125.
[22] EUMANN M, SAUTHOFF G, PALM M. Alloys based on Fe_3Al or FeAl with strengthening Mo_3Al precipitates [J]. Intermetallics, 2004, 12: 625−633.
[23] YILDIRIM M, AKDENIZ M V, MEKHRABOV A O. Effect of ternary alloying elements addition on the order-disorder transformation temperatures of *B*2-type ordered Fe−Al−X Intermetallics [J]. Metallurgical and Materials Transcations A, 2012, 43: 1809−1816.
[24] MEKHRABOV A O, AKDENIZ M V. Effect of ternary alloying elements addition on atomic ordering characteristics of Fe−Al intermetallics [J]. Acta Materialia, 1999, 47: 2067−2075.
[25] KATTNER U R, BURTON B P. Phase diagrams of binary alloys [M]. Materials Park, OH: ASM International, 1993.
[26] YILDIRIM M. Design and development of iron aluminium intermetallic compounds for structural applications at high temperatures [D]. Ankara, Turkey: Middle East Technical University, 2014: 66−69.
[27] XIAO H, BAKER I. The relationship between point defects and mechanical properties in Fe−Al at room temperature [J]. Acta Metallurgica et Materialia, 1995, 43: 391−396.
[28] REIMANN U, SAUTHOFF G. Effects of deviations from stoichiometry on the deformation behaviour of FeAl at intermediate temperatures [J]. Intermetallics, 1999, 7: 437−445.
[29] YILDIRIM M, AKDENIZ M V, MEKHRABOV A O. Microstructural evolution and room-temperature mechanical properties of as-cast and heat-treated $Fe_{50}Al_{50-n}Nb_n$ alloys (n= 1, 3, 5, 7, and 9 at.%) [J]. Materials Science and Engineering A, 2016, 664: 17−25.

添加 Mo 对 Fe−50Al 显微组织、有序度和室温力学性能的影响

Mehmet YILDIRIM[1], M. Vedat AKDENIZ[2], Amdulla O. MEKHRABOV[2]

1. Department of Metallurgical and Materials Engineering, Selcuk University, Konya 42130, Turkey;
2. Novel Alloys Design and Development Laboratory (NOVALAB), Department of Metallurgical and Materials Engineering, Middle East Technical University, Ankara, Turkey

摘　要：研究添加 Mo 对 $Fe_{50}Al_{50-n}Mo_n$ 合金(n=1、3、5、7 和 9，摩尔分数，%)凝固及热处理后的显微组织、位相关系、有序−无序相变温度和室温力学性能的影响。通过 X 射线衍射分析、扫描电镜和差示扫描量热法对材料进行结构表征，通过压缩试验和显微硬度测试研究其室温力学性能。结果显示，所有合金中均有 Mo_3Al 颗粒析出，这是因为 Mo 在 Fe−Al 基相中的固溶度有限。铸态 $Fe_{50}Al_{50-n}Mo_n$ 合金在室温下表现出脆性，具有高的屈服强度和有限的断裂应变。与铸态合金相比，热处理后除了 $Fe_{50}Al_{41}Mo_9$ 合金以外，其他合金的室温力学性能都得到提高。热处理态 $Fe_{50}Al_{43}Mo_7$ 合金具有最高的断裂应变(25.4%)和抗压强度(2.3 GPa)。

关键词：铁铝化合物；显微组织；有序−无序相变；压缩性能

(Edited by Xiang-qun LI)